12^{th} International Conference on Fracture Mechanics of Concrete and Concrete Structures
FraMCoS-12
B.L.A. Pichler, Ch. Hellmich, P. Preinstorfer (Eds)

https://doi.org/10.21012/FC12.1101
PL6

MODELING OF FRACTURE IN BRITTLE AND QUASI-BRITTLE MATERIALS USING GRAPH-BASED FINITE ELEMENT APPROACH

SACHIN VELAYUDHAN*, ARUN R. SRINIVASA**
PRAKASH THAMBURAJA† AND J. N. REDDY‡

*Texas A&M University (TAMU), Department of Mechanical Engineering
College Station, Texas, USA
e-mail: sachin@tamu.edu

**Texas A&M University (TAMU), Department of Mechanical Engineering
College Station, Texas, USA
e-mail: arun-r-srinivasa@tamu.edu

†Universiti Kebangsaan Malaysia (UKM), Department of Mechanical & Manufacturing Engineering
Bangi 43600, Malaysia
e-mail: p.thamburajaukm.edu.my

‡Texas A&M University (TAMU), Department of Mechanical Engineering
College Station, Texas, USA
e-mail: jnreddy@tamu.edu; mechanics.tamu.edu

Key words: Graph-based FEA, Plates, Quasi-Brittle Materials, Nonlocal Constitutive Model, Fracture Modeling, Numerical Results

Abstract. A thermodynamically consistent model for modeling fracture in brittle and quasi-brittle plates is presented. In particular, using the graph-based (GraFEA) approach of the authors to model fracture in two and three-dimensional elastic problems, a GraFEA model that describes the bending kinematics of plates using the first-order shear deformation theory (FSDT) is developed. The fundamental idea of this model is the presence of multiple microcrack planes traversing through a material point on the top and bottom surfaces of the plate. The state of a crack plane evolves based on the probabilistic description of microcracks at the top and bottom half of the plate. An elastic corrector-fracture predictor method and a velocity-verlet algorithm are used to solve the equations governing the bending of plates. It is shown that the proposed formulation compares well with the numerical results from the GraFEA 2D and GraFEA 3D simulations as well as experimental results found in the literature. Complex fracture patterns of plates under static and dynamic loads are predicted within a few minutes on a laptop computer as compared to several hours or days on a supercomputer for a full 3D simulation. A number of numerical examples of plate bending are presented to show the model's robustness.

1 Introduction

Plate-like structures made of glass and concrete are found in many modern buildings and civil and military constructions. They are often subjected to loads transverse to the plane of the plate, which may cause them to develop fracture and ultimately lead to failure. Understanding the structural behavior under such loads is essential for selecting optimal material composition and achieving high energy absorption. Due

to their technological importance, many models for simulating the fracture of quasi-brittle materials have been developed in general (see the review article [1] and the paper by Velayudhan et al. [2]). However, fracture modeling of plates is relatively more recent and can be broadly classified into (1) 3D finite element models [3, 4] that treat plates simply as 3D bodies and (2) finite element models that make use of plate theories with a fracture model based on phase-field, peridynamics, and XFEM approaches (see, e.g., [5–12]). The following brief review of the literature provides the background for the present paper.

There are efforts using a 3D FEA with microplane model [3], GraFEA [4], and Abaqus Concrete Plasticity Damage Model (CDPM) [13] to investigate the fracture process in quasi-brittle materials including plates. However, the key challenge with the fracture simulation of real-world structures is that the computational time is prohibitively large, even with the latest advancements in computation (see, e.g., [3, 6, 14]). These approaches have serious limitations. For example, XFEM and CZM break down when multiple crack paths, such as those seen in quasi-brittle materials [15]. Defining the crack tip field for each crack when multiple cracks develop is a significant computational challenge because it requires prior knowledge of the crack paths. Similarly, phase-field and peridynamics modes have their own limitations and do not consider the different fracture patterns of plate surfaces under bending.

The present approach overcomes these difficulties by proposing a physically motivated and thermodynamically consistent plate model with non-local integral criteria for crack growth. Furthermore, unlike peridynamics, we consider nonlocality only for the damage evolution, not as a constitutive model formulation. Thus, the proposed approach could easily fit into any conventional finite element code or commercial finite element software, such as ABAQUS, LS-DYNA, ANSYS, etc., whose element library has first-order shear deformation plate elements. Thus, the present model is robust and computationally simple, which also captures the physics and topology of microcracking in an efficient way.

2 Theoretical Formulation

2.1 Kinematics

In this section, we briefly review the plate fracture model using the GraFEA framework and small strain-based first-order shear deformation theory [16]. For computational convenience, we write the strains associated with this plate model as,

$$\begin{aligned}\mathbf{E} &= \left[\varepsilon^0_{xx}, \varepsilon^0_{yy}, \gamma^0_{xy}\right]^\intercal - z\left[\varepsilon^1_{xx}, \varepsilon^1_{yy}, \gamma^1_{xy}\right]^\intercal \\ &\equiv \mathbf{E}_m - z\mathbf{G}, \\ \mathbf{E}_s &= \left[\gamma^0_{yz}, \gamma^0_{xz}\right]^\intercal\end{aligned} \tag{1}$$

where $\mathbf{E}_m$ is the membrane strain, $\mathbf{E}_s$ is the shear strain, and $\mathbf{G}$ is the curvature.

2.2 Crack planes

Similar to previous studies on GraFEA [17, 18], we define the *fracture probability* (ϕ^F) of a crack plane i as the probability of finding a microcrack of orientation equal to the crack plane, i, at a material point $\mathbf{x}$ at time t over many samples. For the development of the theoretical framework further, we define the survival probability ($\phi_i = 1 - \phi^F$) of the ith crack plane as the probability of not finding a microcrack of orientation equal to the ith crack plane at a material point $\mathbf{x}$ at time t over many samples. In this model, we define the *survival probability* (ϕ^α_i) of the ith crack plane at a material point $\mathbf{x}$ and at α-surface ($\alpha = t, b$), as the probability of not finding a microcrack of orientation equal to the ith crack plane at the α-half of the plate corresponding to material point $\mathbf{x}$ at time t over many samples. Crack planes (CP) are specified at an angle relative to the x-axis in the 2D plane.

For the transformation of strains and stresses normal to the crack planes, it is convenient to represent the normal vector in the following form:

$$\mathbf{N}^\alpha_i = \left[(n^\alpha_{ix})^2, (n^\alpha_{iy})^2, n^\alpha_{ix} n^\alpha_{iy}\right]^\intercal \tag{2}$$

where $\mathbf{n}^\alpha_i$ ($\alpha = t, b$) represents the normal vector corresponding to i^{th} CP at the top (t) and

bottom (b) plate surfaces; and $\mathbf{N}_i^\alpha$ ($\alpha = t, b$) represent modified crack plane normal (for the i^{th} CP) at the top and bottom surfaces.

2.3 Strain normal to the crack plane and equivalent elastic strain

When the plate deforms, the strain, e_i^α ($\alpha = t, b$) normal to the crack plane i at the top and bottom surface are,

$$e_i^\alpha = \mathbf{N}_i^\alpha \cdot \mathbf{E}^\alpha \tag{3}$$

For mode 1 cracking across the crack plane i, if we consider the probability of finding a microcrack of orientation i at α-surface corresponding to material point $\mathbf{x}$ over all realizations (samples) as $(1 - \phi_i^\alpha)$, the expected value of the crack opening strain across the ith crack plane at the top (d_i^t) and bottom (d_i^b) surfaces can be expressed as

$$d_i^\alpha = (1 - \phi_i^\alpha) \langle e_i^\alpha \rangle \tag{4}$$

where $< y >:= (y + |y|)/2$ is the ramp function. For macroscopic response, given the number of possible crack normals, we need a tensor $\mathbf{H}_\phi^\alpha$ whose components along any crack plane normal is the best approximation to crack opening strain over all realizations ($\mathbf{N}_i^\alpha \cdot \mathbf{H}_\phi^\alpha \approx d_i^\alpha$). Hence, we satisfy this condition in the least square sense and find an expression for $\mathbf{H}_\phi^\alpha$,

$$\begin{aligned}
\mathbf{H}_\phi^\alpha &= argmin_{\mathbf{A}^\alpha} \sum_i \left(||\mathbf{N}_i^\alpha \cdot \mathbf{A}^\alpha - d_i^\alpha||^2 \right) \\
\mathbf{H}_\phi^\alpha &= \sum_{i=1}^{K_\alpha} d_i^\alpha \mathbf{Z}_i^\alpha, \qquad \mathbf{Z}_i^\alpha := \mathbf{B}_\alpha^+ \mathbf{N}_i^\alpha, \\
\mathbf{B}_\alpha &:= \sum_{i=1}^{K} \mathbf{N}_i (\mathbf{N}_i)^\intercal, \quad \mathbf{E}_\phi^\alpha = \mathbf{E}^\alpha - \mathbf{H}_\phi^\alpha,
\end{aligned} \tag{5}$$

where $\mathbf{E}_\phi^\alpha$ is the equivalent elastic strain, $\mathbf{B}_\alpha^+$ is the Moore-Penrose pseudoinverse of the matrix $\mathbf{B}_\alpha$. If the $\mathbf{B}_\alpha$ is non-singular, $\mathbf{B}_\alpha^+ = \mathbf{B}_\alpha^{-1}$.

The effective membrane strain ($\mathbf{E}_m^e$) and effective curvature ($\mathbf{G}^e$) are defined using the equivalent elastic strain as

$$\begin{aligned}
\mathbf{E}_m^e &\equiv \frac{1}{2}\left(\mathbf{E}_\phi^t + \mathbf{E}_\phi^b\right) = \mathbf{E}_m - \frac{1}{2}\left(\mathbf{H}_\phi^t + \mathbf{H}_\phi^b\right), \\
\mathbf{G}^e &\equiv \frac{1}{2h}\left(\mathbf{E}_\phi^t - \mathbf{E}_\phi^b\right) = \mathbf{G} - \frac{1}{2h}\left(\mathbf{H}_\phi^t - \mathbf{H}_\phi^b\right)
\end{aligned} \tag{6}$$

where $2h$ is the total thickness of the plate. This effective membrane strain and effective curvature are assumed to be (at least approximately) the membrane strain and curvature in the plate at the same state of stress if there are no cracks.

Figure 1 illustrates the crack growth in a quasi-brittle material under pure bending.

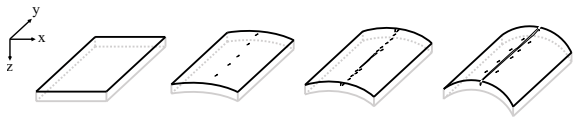

Figure 1: When the plate undergoes pure bending, the crack at the top surface of the plate opens and propagates up to the neutral surface of the plate. In a quasi-brittle material, microcracks are developed on the plate surfaces initially and then coalesced to form a macro-crack upon continuous loading.

2.4 Constitutive model

We define the isothermal Helmholtz potential as a quadratic function of effective membrane strain, effective curvature, and shear strain. After integrating through the plate thickness, the Helmholtz potential per unit area can be expressed as follows:

$$\begin{aligned}
\Psi &= \Psi_m(\mathbf{E}_m^e) + \Psi_k(\mathbf{G}^e) + \Psi_s(\mathbf{E}_s) \\
\Psi &= \frac{1}{2}\mathbf{E}_m^e \cdot [A_m]\mathbf{E}_m^e + \frac{1}{2}\mathbf{G}^e \cdot [D]\mathbf{G}^e \\
&\qquad + \frac{1}{2}\mathbf{E}_s \cdot [A_s]\mathbf{E}_s \\
([A_m]\mathbf{E}_m^e)^\intercal &= \hat{\mathbf{N}}, \qquad ([D]\mathbf{G}^e)^\intercal = \hat{\mathbf{M}}
\end{aligned} \tag{7}$$

The plate constitutive relations are obtained by differentiating the Helmholtz potential with respect to the membrane strain, curvature, and transverse shear strain (not given here; see [2]).

The driving force for the evolution of survival probability is the change in Helmholtz potential with the change in the crack plane survival probability. Hence, driving force per unit

length across the ith crack plane at the top surface (P_i^t) and the jth crack plane at the bottom surface (P_j^b) are (no summation over i and j),

$$\begin{aligned} P_i^t &= \frac{\partial \Psi}{\partial \phi_i^t} = \frac{1}{2}\left\{\hat{\mathbf{N}} + \frac{1}{h}\hat{\mathbf{M}}\right\}\left(\mathbf{Z}_i^t \left\langle e_i^t \right\rangle\right), \\ P_j^b &= \frac{\partial \Psi}{\partial \phi_j^b} = \frac{1}{2}\left\{\hat{\mathbf{N}} - \frac{1}{h}\hat{\mathbf{M}}\right\}\left(\mathbf{Z}_j^b \left\langle e_j^b \right\rangle\right) \end{aligned} \tag{8}$$

With this notation (details are omitted), the isothermal form of the Clausius-Duhem inequality reduces to

$$-\sum_{i=1}^{K_t} P_i^t \dot{\phi}_i^t - \sum_{j=1}^{K_b} P_j^b \dot{\phi}_j^b = \xi \geq 0 \tag{9}$$

2.5 Nonlocal strain and survival probability evolution

The fundamental qualitative notion of damage in quasi-brittle materials is that it starts from existing flaws like voids or cracks, leading to gradual and stable microcrack growth, influenced by stress shielding from neighboring microcracks. This region is called the Fracture Process Zone (FPZ). Since we do not know precisely the conditions near the microcracks in the FPZ, we follow the probabilistic description of the state of a crack plane and its evolution based on the formulation described by Srinivasa et al. [17] and Thamburaja et al. [18]. As noted before, the probability that a potential microcrack plane in the FPZ will transition from intact to fractured is defined by an equation for the evolution of survival probability of a crack plane:

$$\dot{\phi}_i^\alpha = -T_i^\alpha(\text{intact} \to \text{fractured})\phi_i^\alpha \tag{10}$$

Thus, the damage evolution is governed by the transition probability function from intact to fractured, and it contains the (qualitative) physics of the fracture process. Thus, we assume the transition probability function for the top and bottom surfaces of the plate as,

$$T_i^\alpha = T_0 \mathcal{H}(P_i^\alpha)\mathcal{H}(e_i^\alpha)\left\langle \left(\frac{I_i^\alpha}{(I_i^c)^\alpha} - 1 \right) \right\rangle \langle \dot{e}_i^\alpha \rangle \tag{11}$$

where T_0 is the softening rate parameter, $(I_i^c)^\alpha$ is the rate-dependent threshold strain and I_i^α is the nonlocal influence on strain across the crack plane i.

The nonlocal strain at material point **x** can be written as [see Eq. (2.3) in [19]],

$$\bar{\mathbf{E}}^\alpha(\mathbf{x}) = \left\{ \int_{\mathcal{R}_f} \mathcal{H}\left(r_\phi - |\mathbf{x}-\mathbf{y}|\right) \phi_i^\alpha(\mathbf{x})\omega^\alpha(\mathbf{y})\mathbf{E}^\alpha(\mathbf{y}) dA \right\} \frac{1}{\bar{A}^\alpha(\mathbf{x})} \tag{12}$$

where

$$\begin{aligned} \bar{A}^\alpha(\mathbf{x}) &= \int_{\mathcal{R}_f} \mathcal{H}\left(r_\phi - |\mathbf{x}-\mathbf{y}|\right)\omega^\alpha(\mathbf{y}) dA, \\ \omega^\alpha(\mathbf{y}) &:= \frac{1}{K_\alpha}\sum_{i=1}^{K_\alpha} \phi_i^\alpha(\mathbf{y}) \end{aligned} \tag{13}$$

The product $\omega^\alpha(\mathbf{y})\mathbf{E}^\alpha$ represents the effect of shielding from the neighboring cracks since it is zero when all neighboring cracks are fractured, and there are no new potential cracks.

We assume that the rate-dependent threshold strain follows a power-law expression as [17, 18],

$$(I_i^c)^\alpha = I_0^c \left\{ 1 + \mathcal{H}(\dot{e}_i^\alpha - \dot{e}_0)\left[\left(\frac{\dot{e}_i^\alpha}{\dot{e}_0} \right)^{c_0} - 1 \right] \right\} \tag{14}$$

where I_0^c is the rate-independent threshold strain, c_0 is the power-law coefficient, and $\dot{e}_0$ is the threshold strain rate.

2.6 Finite element model

We use four-node quadrilateral and linear triangular elements to discretize the computational domain (to solve plane stress problems and compare them with GraFEA 2D only). The generalized displacements are the three midsurface displacements and two rotations about the inplane coordinates. The Lagrange interpolation of the five displacements is used. We solve for the nodal displacements during the elastic predictor stage of the solution methodology (see [2] for the solution procedure). Therefore, the survival probability remains constant when the stiffness matrix is derived. Hence, the nodal

force and stiffness matrix can be obtained directly from the Helmholtz potential (see [2] for details) as follows:

$$\mathbf{F} = \frac{\partial \Psi}{\partial \mathbf{u}} = ([A_m]\mathbf{E}_m^e)^\intercal \frac{\partial \mathbf{E}_m^e}{\partial \mathbf{u}} + ([D]\mathbf{G}^e)^\intercal \frac{\partial \mathbf{G}^e}{\partial \mathbf{u}} + ([A_s]\mathbf{E}_s)^\intercal \frac{\partial \mathbf{E}_s}{\partial \mathbf{u}} \tag{15}$$

We derive the stiffness matrix by differentiating nodal forces with respect to the generalized displacements and obtain

$$\mathbf{K} = \frac{\partial \mathbf{F}}{\partial \mathbf{u}} = \left([A_m]\frac{\partial \mathbf{E}_m^e}{\partial \mathbf{u}}\right)^\intercal \frac{\partial \mathbf{E}_m^e}{\partial \mathbf{u}} + \left([D]\frac{\partial \mathbf{G}^e}{\partial \mathbf{u}}\right)^\intercal \frac{\partial \mathbf{G}^e}{\partial \mathbf{u}} + \left([A_s]\frac{\partial \mathbf{E}_s}{\partial \mathbf{u}}\right)^\intercal \frac{\partial \mathbf{E}_s}{\partial \mathbf{u}} \tag{16}$$

3 Numerical Results

Since the experimental works [20–23] have not provided enough details to calibrate and validate the plate fracture model, we use GraFEA 2D and 3D to verify the plate model (a validation of GraFEA is provided in [4, 24]).

3.1 Plate with a hole subjected to tension

We verify the proposed plate fracture model and its computational framework by comparing the response of a 2D fracture problem with that obtained with the GraFEA 2D. We chose a plate with a hole subjected to tension here. Only half-plate is modeled in both the plate fracture model and GraFEA 2D [see Figure 2(a)]. The boundary conditions applied are: (a) The nodes on the right vertical edge are constrained from the motion in the x-direction (i.e., $u = 0$); (b) the nodes located at the top horizontal edge are imposed a constant velocity of 1.0×10^{-3} mm/s in the y-direction; and (c) the nodes located at the bottom horizontal edge are constrained from the motion in the y-direction (i.e., $v = 0$). The material parameters illustrated in Table 1 (corresponding to GraFEA 3D) are assumed for the plate fracture model and GraFEA 2D. The computational domain is discretized using linear triangular elements, and three crack planes oriented at a relative angle of 60° are considered. A local simulation is performed, and an element size equal to the nonlocal zone size is considered in both cases.

Figure 2 illustrates the average survival probability contour from the GraFEA 2D and plate fracture model at each Gauss point. The crack initiated at the hole tip and propagated toward the opposite edge of the plate [See Figure 2(b) and (c)]. The survival probability of the crack planes at the top and bottom surfaces of the plate remained the same under this extensional fracture mode in the plate fracture model. The applied displacement at the top nodes versus total reaction force response from the GraFEA 2D and plate fracture model is illustrated in Figure 2(d). The load-displacement response and average survival probability contours obtained with the plate fracture model agree with those of the GraFEA 2D. The governing equations of motion are solved using the velocity-verlet algorithm. These results verified that the plate fracture model reduces to GraFEA 2D when subjected to a simple tension.

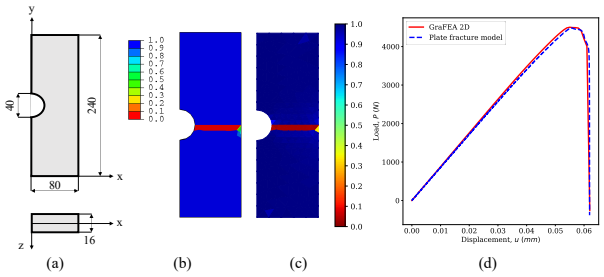

Figure 2: (a) A rectangular plate of in-plane dimensions 80 mm $\times$ 240 mm, thickness of 16 mm, a hole radius of 20 mm, fixed at the bottom edge, and subjected to tensile load at the top surface. (b) The average survival probability at the front face of the plate from GraFEA 2D. (c) The average survival probability at the front face from the Plate fracture model. Both simulations predicted the same fracture topology. (d) The applied displacement versus total reaction force at the top edge of the plate from GraFEA 2D and plate fracture model. The same material properties, mesh, and crack plane orientations are assumed in the GraFEA 2D and Plate Fracture model for this simulation.

3.2 Calibration of model parameters

We use the following strategy to calibrate the material parameters of the plate fracture

model: perform the cantilever plate local simulation with and without loading rate effects and nonlocal simulation with loading rate effects using GraFEA 3D, as illustrated in Figure 3(a). The material parameters for High Strength Concrete (HSC) illustrated in Table 1 are used for GraFEA 3D simulation [24]. A square plate of side 50 mm and thickness of 10 mm, fixed at the left edge and subjected to shear load on the right edge, is considered [see Figure 3(a)]. In GraFEA 3D, the boundary conditions imposed are: (a) the nodes at the left face are constrained from all the displacements, and (b) the nodes at the top edge of the right-side face are subjected to a constant velocity of 1.5×10^{-3} mm/s in the y-direction. In the plate fracture model, we apply the same boundary conditions at the left and right edges of the plate. In GraFEA 3D, we discretize the computational domain using linear tetrahedral elements, and six crack planes are assumed to orient perpendicular to the element edges.

We use the following strategy to fit the material parameters in the plate fracture model:

1. We perform local simulation (using the plate fracture model) without loading rate effects. Hence, in this simulation, the threshold strain rate for a rate-dependent cohesive response is assumed to be very high to ensure that the deformation is independent of the loading rate. The load versus displacement curve from the plate fracture model is fitted against the results from GraFEA 3D by varying only the softening rate parameter (T_0) [see Figure 3(b)].

2. Next, we fit the dimensionless power law coefficient (c_0) and threshold strain rate ($\dot{e}_0$) for rate-dependent cohesive response by comparing the load-displacement curve from GraFEA 3D and the plate fracture model local simulation with loading rate effects. The displacement applied is plotted against the total reaction force in both cases [see Figure 4(a)]. The dimensionless power law coefficient and threshold strain rate (see Equation No: 14) remain the same as the values used for the GraFEA 3D simulation.

3. Using the plate fracture model, we perform a nonlocal simulation with loading rate effects. We calibrated the correction factor (c_f) multiplied with the nonlocal strain by fitting the load-displacement response from the plate fracture model with the GraFEA 3D response [see Figure 4(b)]. The final material parameters and nonlocal strain correction factor are presented in Table 1. Since we use the same thickness to nonlocal zone size ratio for all the boundary value problems in the following subsections, we assume the same nonlocal strain correction factor fitted here.

Table 1: Calibrated material parameters with rate effects.

Material Constants	GraFEA3D	Plate model
Shear Modulus (MPa)	7.5×10^3	7.5×10^3
Bulk Modulus (MPa)	10×10^3	10×10^3
Rate-independent threshold strain (I_0^c)	1.3×10^{-4}	1.3×10^{-4}
Nonlocal zone radius (r_ϕ)	4.5 mm	4.5 mm
Power law coefficient (c_0)	0.055	0.055
Softening rate parameter (T_0)	450.0	180.0
Threshold strain rate ($\dot{e}_0$)	3×10^{-6}	3×10^{-6}
Nonlocal strain correction factor (c_f)	-	0.54

A nonlocal zone of a sphere with a radius of 4.5 mm is considered in GraFEA 3D with an element size equal to 1.8 mm. This ensures a minimum of 5 elements through the diameter of the nonlocal zone. We demonstrate the capability of the plate fracture model with both coarse (with the element size equal to the nonlocal zone size) and fine mesh (with the element size

equal to one-fifth of the nonlocal zone size). In the plate fracture model, we discretize the computational domain using four-node quadrilateral elements and crack planes oriented at $(0°, 45°, 90°, 135°)$ with the horizontal axis.

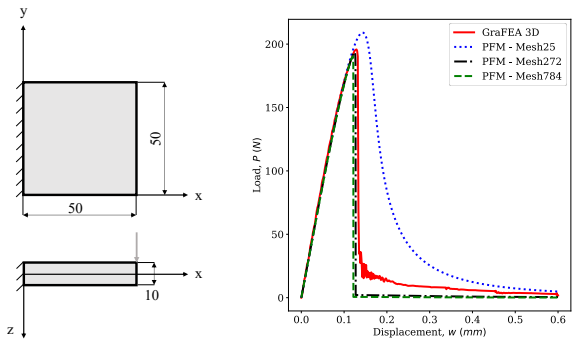

Figure 3: (a) A square plate of side 50 mm, thickness 10 mm, clamped on the left edge, and shear load applied at the right edge. (b) The load versus displacement response obtained from GraFEA 3D and plate fracture simulation. The softening rate parameter (T_0) is calibrated to fit the load versus displacement curve.

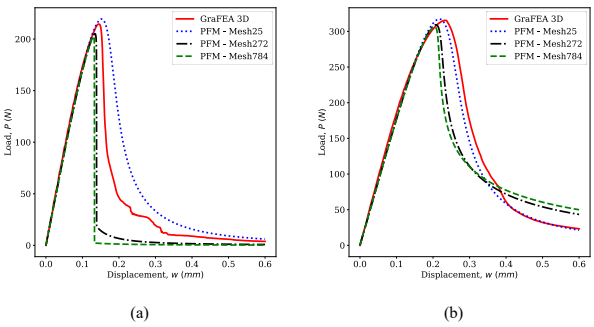

Figure 4: The load versus displacement response obtained from GraFEA 3D and plate fracture simulation. (a) Performed a loading-rate-dependent simulation. The dimensionless power law coefficient and threshold strain rate used in the plate fracture model remain the same as the values used for the GraFEA 3D simulation. (b) Performed a nonlocal simulation in GraFEA 3D and plate fracture model. Introduced a correction factor in the plate fracture model for the nonlocal strain calculation to fit the load versus displacement curve. The fitted material parameters for the plate fracture model are illustrated in Table 1.

3.3 Independent prediction and verification using GraFEA 3D

Next, we predict the failure and load-displacement response under a three-point bend test using the calibrated material parameters from the previous section. We use a support span of 80 mm and half of the geometry by assuming symmetry boundary conditions to perform this simulation [see Figure 5(a)]. In GraFEA 3D and plate fracture model, we apply the boundary conditions directly to the nodes where (a) a constant velocity of 1.5×10^{-3} mm/s is applied at the nodes below the top punch head in the z-direction, (b) the displacement at the nodes above support is constrained in the z-direction, and (c) symmetry boundary condition ($u = r_x = 0$) at the nodes below the top punch head. In the plate fracture model, all the boundary conditions are applied at the nodes at the mid surface of the plate.

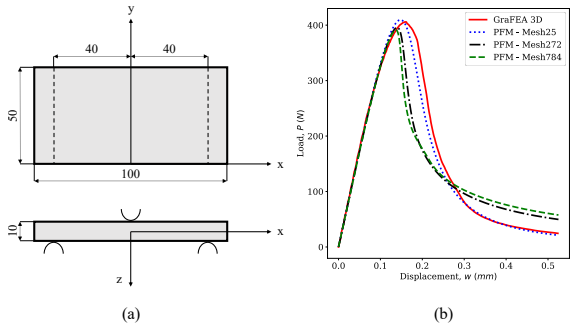

Figure 5: (a) Three-point bend test on a rectangular plate of size 100 × 50 mm and thickness 10 mm. The boundary conditions are directly applied at the nodes and a constant velocity is imposed at the nodes below the top punch head. We used half domain for the fracture simulation. (b) The load versus displacement response obtained from GraFEA 3D and plate fracture models. The plate fracture model results show good agreement with GraFEA 3D results with the peak load and steady-state load predicted within 5% range.

The crack planes are assumed to orient perpendicular to the element edges in GraFEA 3D, whereas the plate fracture model considers four crack planes with a relative angle of $45°$. Table 1 illustrates the material parameters for GraFEA 3D and plate fracture nonlocal simulations considered for the simulation. We sim-

ulate the plate fracture model using coarse and fine mesh. Figure 5(b) illustrates the displacement applied versus total reaction force from GraFEA 3D and plate fracture simulation. We can see that the plate fracture model predicts the GraFEA 3D-determined load-displacement response well. The peak load and steady-state load predicted by the plate fracture model are within the 5% range compared to the GraFEA 3D result.

4 Comparison of crack topology with experiments

In this section, we demonstrate the capabilities of the plate fracture model by comparing against the experimental results. The coaxial double-ring test [25] and ball-on-three-ball test [26] are standard tests for finding equi-biaxial flexure strength. We chose the ball-on-three-ball test on cement mortar [23] to compare the crack topology in this work. In this simulation, six crack planes that are oriented at a relative angle of 30° are considered at each Gauss point.

Turker [23] has investigated the size effect and biaxial flexure strength of Portland cement mortar with fine aggregates by performing a ball-on-three-balls test and triangular plate method. In this study, different-sized triangular samples are considered and supported below by three balls placed at 120° relative angle as shown in Figure 6(a). Turker [23] placed the three balls far from the side to avoid crack growth to the side from the support balls. The load is applied using another ball at the center. The cracks are observed between the support pivots and the center of the plate, breaking the sample into two or three [see Figure 6(b) and 6(c)]. The plate fracture simulation was carried out by considering an equilateral triangle plate of side 400 mm and thickness of 20 mm. The boundary conditions imposed on the plate are: (a) nodes above the support balls are constrained from the motion in the z-direction, (b) node below the load ball is constrained from motion in the x and y-direction, and (c) a constant velocity of 7.5×10^{-4} mm/s is imposed at the node below load ball in the z-direction. The material parameters corresponding to GraFEA 3D in Table 1 are used. Initially, one major crack is observed, splitting the sample into two as illustrated in Figure 6(d). However, with continued loading, cracks grow in the area between the support balls, splitting the sample into three pieces [see Figure 6(e)]. The stress is equi-biaxial at the center of the plate's bottom surface, as expected.

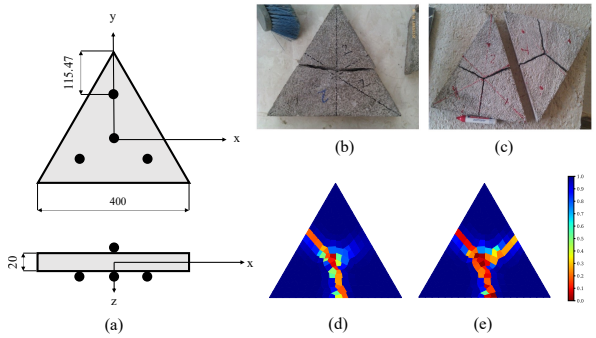

Figure 6: (a) Ball-on-three-ball test on an equilateral triangular plate of side 400 mm and thickness 20 mm. The three support balls are placed at 120° relative angle and one-third distance of the bisector from the vertex to the opposite edge. (b) The sample broke into two pieces under the ball-on-three-ball test [23]. (c) Triple cracks are observed in most of the samples from the experiments performed by Turker [23]. (d) The average survival probability at the plate bottom surface. One straight crack was observed initially. (e) The average survival probability at the plate bottom surface when the load was continuously applied after observing one straight crack.

5 Summary and Conclusions

In this work, an approach to investigate the fracture of quasi-brittle plate structures using the FSDT kinematics and GraFEA is presented. An in-house C++ code was developed based on the quasi-static and dynamic version of the finite element framework derived from the theoretical formulation described. The computational framework was initially verified by comparing the structural response with GraFEA 2D. We then calibrated the model parameters in the plate fracture model using GraFEA 3D simulations by performing a cantilever plate simulation. Subsequently, the plate response

when subjected to a three-point bend test was independently predicted and compared with GraFEA 3D results. We qualitatively compared the crack topology predicted by the plate fracture model with the experiments conducted on cement mortar samples [23]. The model presented was able to predict the response of plate structures, comparing well with GraFEA 2D, 3D, and experiments. The model needs to be improved to capture the through-the-thickness crack propagation by modifying the neutral surface location under bending when the crack grows from the tensile to the compressive surface of the plate.

Acknowledgments

The authors acknowledge the use of the Texas A&M University (TAMU) High Performance Research Computing center for the computing resources. S. V. Acknowledges the support from the O'Donnell Foundation Chair IV, A.S. and J. N. R. acknowledge support received from Holdredge/Paul Professorship and the O'Donnell Foundation Chair IV, respectively. **The last author dedicates this paper to the legacy of Professor Kasper Willam.**

REFERENCES

[1] Shin, Ho Yong and Lawrence, Carson and Kota, Kalyan Raj and Thamburaja, Prakash and Srinivasa, Arun and Lacy Jr, Thomas E and Reddy, J. N. 2022. Experimental, theoretical and numerical studies on plain concrete fracture in the low-strain rate regime—A state-of-the-art review. *Mechanics of Advanced Materials and Structures* **29**(28): 7115–7159.

[2] Velayudhan, Sachin, Srinivasa, A. R., Thamburaja, P., and Reddy, J. N. 2025. Modeling of fracture in plates using a Graph-Based Finite Element Analysis (GraFEA). *ASCE Journal of Engineering Mechanics* (in review).

[3] Kirane, Kedar, Bažant, Zdeněk P., and Zi, Goangseup. 2014. Fracture and size effect on strength of plain concrete disks under biaxial flexure analyzed by microplane model. *Journal of Engineering Mechanics* **140**(3):604–613,

[4] Shin, H. Y., Thamburaja, P., Srinivasa, A. R., and Reddy, J. N. 2023. Modeling impact fracture in a quasi-brittle solids using a 3D nonlocal graph-based finite element analysis: Theory, finite element simulations, and experimental verification *Journal of the Mechanics and Physics of Solids* **170**:105097,

[5] Areias, Pedro, Rabczuk, Timon, and Msekh, M. A. 2016. Phase-field analysis of finite-strain plates and shells including element subdivision. *Computer Methods in Applied Mechanics and Engineering* **312**:322–350.

[6] Liu, Zeng, Reinoso, J., and Paggi, Marco. 2022. Phase field modeling of brittle fracture in large-deformation solid shells with the efficient quasi-Newton solution and global–local approach. *Computer Methods in Applied Mechanics and Engineering* **399**:115410.

[7] Raghu, P., Rajagopal, Amirtham, and Reddy, J. N. 2020. Thermodynamically consistent variational approach for modeling brittle fracture in thick plates by a hybrid phase field model. *Journal of Applied Mechanics* **87**(2):021002.

[8] Chowdhury, Shubhankar Roy and Roy, Pranesh and Roy, Debasish and Reddy, J. N. 2016. A peridynamic theory for linear elastic shells. *International Journal of Solids and Structures* **84**:110–132.

[9] Diyaroglu, Cagan, Oterkus, Erkan, Oterkus, Selda and Madenci, Erdogan. 2015. Peridynamics for bending of beams and plates with transverse shear deformation. *International Journal of Solids and Structures* **69**: 152–168,

[10] Larsson, Ragnar, Mediavilla, Jesus, and Fagerström, Martin. Dynamic fracture modeling in shell structures based on

XFEM. 2011. *International Journal for Numerical Methods in Engineering* **86**(4-5): 499–527.

[11] Areias, Pedro M. A. and Belytschko, T. 2005. Non-linear analysis of shells with arbitrary evolving cracks using XFEM. 2005. *International Journal for Numerical Methods in Engineering* **62**(3):384–415.

[12] Dolbow, John, Moës, Nicolas, and Belytschko, T. 2000. Modeling fracture in Mindlin–Reissner plates with the extended finite element method. *International Journal of Solids and Structures* **37**(48-50):7161–7183.

[13] Nguyen, Tuan H. A. and Niiranen, Jarkko. 2021. Nonlocal continuum damage modeling for functionally graded plates of third-order shear deformation theory. *Thin-Walled Structures* **164**:107876,

[14] Guojun, Zheng, Runjin, Li, Guozhe, Shen and Xiangkui, Zhang. 2024. A parallel acceleration GPU algorithm for large deformation of thin shell structures based on peridynamics. *Engineering with Computers* **40**:3009–3030.

[15] Khodabakhshi, Parisa, Reddy, J. N., and Srinivasa, Arun 2016. GraFEA: a graph-based finite element approach for the study of damage and fracture in brittle materials. *Meccanica* **51**:3129–3147,

[16] Reddy, J. N. 2014. *An Introduction to Nonlinear Finite Element Analysis: with Applications to Heat Transfer, Fluid Mechanics, and Solid Mechanics*, Oxford University Press, Oxford, UK (2nd ed.).

[17] Srinivasa, A. R., Shin, H. Y., Thamburaja, P., and Reddy, J. N. 2021. Multiple cracking model in a 3D GraFEA framework. *Continuum Mechanics and Thermodynamics* **33**:1409–1428,

[18] Thamburaja, P., Sarah, K., Srinivasa, A., and Reddy, J. N. 2021. Fracture modelling of plain concrete using non-local fracture mechanics and a graph-based computational framework. *Proceedings of the Royal Society A* **477**(2252):20210398,

[19] Bažant, Zdeněk P. and Pijaudier-Cabot, Gilles. 1988. Nonlocal Continuum Damage, Localization Instability and Convergence *Journal of Applied Mechanics* **55**(2):287-293,

[20] Castori, Giulio and Speranzini, Emanuela. 2019. Fracture strength prediction of float glass: The coaxial double ring test method. *Construction and Building Materials* **225**:1064–1076.

[21] Zi, Goangseup, Kim, Jihwan, and Bažant, Zdeněk P. 2014. Size effect on biaxial flexural strength of concrete. *ACI Materials Journal* **111**(3):319–326.

[22] Zi, Goangseup, Oh, Hongseob, and Park, Sun-Kyu. 2008. A novel indirect tensile test method to measure the biaxial tensile strength of concretes and other quasibrittle materials. *Cement and Concrete Research* **38**(6):751–756

[23] Turker, Hakan T. 2022. Effect of size on biaxial flexural strength for cement-based materials by using a triangular plate method. 2022. *Frontiers of Structural and Civil Engineering* **16**(8):1017–1028.

[24] Shin, H. Y., Thamburaja, P., Srinivasa, A. R., and Reddy, J. N. 2022. On simulating impact fracture in high-strength concrete using GraFEA. *Extreme Mechanics Letters* **52**:101618

[25] Standard test method for monotonic equibiaxial flexural strength of advanced ceramics at ambient temperature. Technical Report ASTM C1499-19, 2019.

[26] Standard test method for flexural toughness of fiber reinforced concrete (using centrally loaded round panel). Technical Report ASTM C1550-20, 2020.